

# **Hemoglobin-derived Fe-N<sub>x</sub>-S species supported by bamboo-shaped carbon nanotubes as efficient electrocatalysts for the oxygen evolution reaction**

Weiming Chen <sup>a, 1</sup>, Xuanli Luo <sup>c, 1</sup>, Sanliang Ling <sup>c</sup>, Yongfang Zhou <sup>a</sup>, Bihan Shen <sup>a</sup>, Thomas J A Slater <sup>d</sup>, Jesum Alves Fernandes <sup>e</sup>, Tingting Lin <sup>a</sup>, Jianshe Wang <sup>f</sup>, Yi Shen <sup>a, b \*</sup>

<sup>a</sup> School of Food Science and Engineering, South China University of Technology, Guangzhou, 510641, China.

<sup>b</sup> Overseas Expertise Introduction Center for Discipline Innovation of Food Nutrition and Human Health (111 Center), Guangzhou, 510641, China

<sup>c</sup> Advanced Materials Research Group, Faculty of Engineering, University of Nottingham, Nottingham, NG7 2RD, United Kingdom

<sup>d</sup> Electron Physical Sciences Imaging Centre, Diamond Light Source Ltd., Oxfordshire OX11 0DE, United Kingdom

<sup>e</sup> School of Chemistry, University of Nottingham, Nottingham, United Kingdom

<sup>f</sup> School of Chemical Engineering and Energy, Zhengzhou University, Zhengzhou 450001, China

<sup>1</sup> The two authors contributed equally to this work

---

\* Corresponding author. Email: [feyshen@scut.edu.cn](mailto:feyshen@scut.edu.cn) (Yi Shen)

## Abstract

Herein, we report a facile route to synthesize isolated single iron atoms on nitrogen-sulfur-codoped carbon matrix via a direct pyrolysis process in which hemoglobin, a by-product of the meat industry, was utilized as a precursor for iron, nitrogen and sulfur while bamboo-shaped carbon nanotubes served as a support owing to their excellent conductivity and numerous defects. The resulting metal-nitrogen complexed carbon showed outstanding catalytic performance for the oxygen evolution reaction (OER) in alkaline solutions. At an overpotential of 380 mV, the optimal sample yielded a current density of 83.6 mA cm<sup>-2</sup>, which is 2.5 times that of benchmark IrO<sub>2</sub> (32.8 mA cm<sup>-2</sup>), rendering it as one of the best OER catalysts reported so far. It also showed negligible activity decay in alkaline solutions during long-term durability tests. Control experiments and X-ray absorption fine structure analyses revealed that Fe-N<sub>x</sub> species in the samples are the active sites for OER. Further density functional theory calculations indicated that the presence of sulfur in the carbon matrix modified the electronic structures of active species, thereby leading to the superior activity of the sample.

**Keywords:** *Single-site catalysts; sulfur doping; Fe-N<sub>x</sub>; oxygen evolution reaction; carbon nanotubes*

## 1. Introduction

Molecular hydrogen is an ideal candidate for replacing fossil fuels because of its environmental-friendliness and high energy efficiency [1]. Electrochemical water splitting via the hydrogen evolution reaction (HER) and oxygen evolution reaction (OER) represents a promising approach for hydrogen production [2-5]. Owing to the sluggish kinetics and high overpotentials, the OER is considered to be the bottleneck for water splitting. It necessitates the utilization of high-performance electrocatalysts to maximize energy efficiency. Currently, IrO<sub>2</sub> and RuO<sub>2</sub> are regarded as state-of-the-art OER electrocatalysts. Unfortunately, the scarcity and cost of these precious metal oxides greatly prevent their large-scale application in OER. Searching for high-performance and cost-effective electrocatalysts is thus of great significance for the widespread application of water-splitting techniques [6-9].

Recently, single-atom catalyst (SAC) has triggered enormous interest owing to their maximum atom efficiency, outstanding activity and selectivity [10-12], and tunable coordination structures [13,14]. Among the reported SAC, metal-nitrogen complexed carbon (MNC) materials are of particular interest for electrocatalysis because of their excellent conductivity [15-19]. So far, MNC has been used in electrochemical processes, such as the oxygen reduction reaction [20,21], HER [22,23], OER [24-26], and CO<sub>2</sub> reduction reaction [27]. The cost-effective and large-scale production of MNC hold the key to their practical applications. Unfortunately, the extremely high surface energy of single metal atoms always leads to natural aggregation into nanoparticles which are catalytically less active than SAC, and this represents a grand challenge for the synthesis of MNC. Currently, pyrolysis of metal salts with nitrogen/carbon precursors has been extensively employed for the synthesis of MNC [28-30]. This synthesis protocol involves high pyrolysis temperatures to yield conductive carbonaceous supports, which unfortunately leads to metal aggregation due to the weak interaction of the metal cations with N/C precursors, greatly reducing the number of single atoms. Such a trade-off relationship between conductivity and the number of catalytically active single atoms greatly affects the performance of the

resulting MNC. Alternatively, metal organic framework (MOF) consisting of metal sites coordinated by N-containing ligands is a better precursor for MNC synthesis [31-34]. However, to facilitate a strong interaction of metals with surrounding ligands in MOF, the choices of metal type and ligands are limited, not to mention that the synthesis of MOF is costly and time-consuming, which significantly prohibits the scalable production of MNC [35]. Thus, the development of cost-effective synthesis methods is still highly desirable to realize the large-scale production of SAC.

The catalytic performance of MNC is closely related to the local geometric and electronic structures of  $M-N_x$  sites. It has been demonstrated that metal atoms in MNC catalysts always exhibit unsatisfactory adsorption-desorption behaviors toward intermediates owing to the electron depletion arising from the interaction of neighboring N atoms, thus increasing the potential barriers of the catalytic reactions [36-39]. The electronic structures of the metals can be further tuned by introducing proper foreign atoms such as sulfur in the carbonaceous matrix [34-36]. Inspired by these results, herein, we report a simple route for the synthesis of MNC via pyrolysis of a mixture of hemoglobin (Hb) and bamboo-shaped carbon nanotube (BCNT). Being the major content of animal blood which can be obtained as a by-product of the meat industry [40], Hb is composed of globin and heme. The former has sulfur elements while the latter contains  $Fe-N_5$  moieties. Such abundant availability and structural features render Hb to be an ideal precursor for the synthesis of MNC. BCNT was utilized as a catalyst support owing to their excellent conductivity and abundant defects [41]. The contents of iron and nitrogen were readily optimized by varying the Hb content in the feedstock and pyrolysis temperature. High-angle annular dark field scanning transmission electron microscopy (HAADF-STEM) confirmed the presence of abundant single iron atoms. X-ray absorption fine structure analyses revealed that the iron atoms were coordinated with nitrogen atoms. The optimal sample showed remarkable OER activity in alkaline solutions and outperformed precious  $IrO_2$  at high overpotentials. Density functional theory (DFT) calculations were conducted to investigate the critical role of sulfur dopant. The superior OER performance was mainly attributed to the abundant  $Fe-N_x$  sites and the promoting role of sulfur.

## 2. Experimental section

### 2.1. Materials

Nafion solution (5 wt.%) was purchased from the Sunlaite Co. Ltd. (Kunshan, China). Isopropanol and ethylene glycol were provided by the Qiangsheng Chemical Reagent Co. Ltd. (Jiangsu, China) and Fuyu Chemical Reagent Co. Ltd. (Tianjin, China), respectively. Hemoglobin was purchased from the Yuanye Biotechnological Co. Ltd. (Shanghai, China). All the chemicals were of analytic grade and were used as received without further purification.

### 2.2. Synthesis of BCNT

BCNT was obtained from a typical process of thermocatalytic decomposition of methane using nickel-copper alloy as a catalyst and further purified by refluxing in a solution of concentrated sulfuric and nitric acids at 140°C overnight as reported in the authors' previous work [42,43]. After cooling to ambient temperature, the mixture was ultrasonicated for 60 min. Afterwards, the BCNT were thoroughly rinsed with deionised water to remove the impurities and dried at 100 °C for further use.

### 2.3. Synthesis of Hb/BCNT

Typically, 800 mg of hemoglobin (Hb) and 200 mg of purified BCNT were dispersed in 5 mL of deionised water by ultrasonication. The resulting mixture was transferred into a vacuum oven. The pressure of the oven was held at 0.01 MPa for 10 min and then recovered to ambient pressure. To facilitate the adsorption of Hb onto the BCNT, the vacuum process was repeated twice. Subsequently, the mixture was dried at 80 °C for 24 h, ground and transferred into a tube furnace. The furnace was heated to a given temperature with a rate of 5 °C min<sup>-1</sup> under nitrogen atmosphere and held at temperature for 2 h. After cooling to ambient temperature, a black powdered product was obtained and denoted as Hb/BCNT-1000. The samples synthesized at varying Hb contents and pyrolysis temperatures were denoted as x%Hb/BCNT-T for convenience, where x% is the weigh percentage of Hb in the mixture and T is the pyrolysis temperature. For

comparison, the sample was also prepared at 1000 °C in the absence of BCNT and denoted as Hb-1000.

#### *2.4. Structural Characterization*

The morphology of the samples was studied by field emission scanning electron microscopy (FESEM) (JSM-7600F, JEOL) and transmission electron microscopy (TEM) (JEM2010, JEOL). To observe the single atoms in the samples, high-angle annular dark field STEM micrographs were obtained from an alternative microscope (ARM200F JEOL) at the Electron Physical Sciences Imaging Centre at Diamond Light Source. An acceleration voltage of 200 kV was used throughout the measurements, with a beam current of approximately 15 pA, a convergence semi-angle of 23 mrad and a high-angle annular dark field (HAADF) inner angle of 80 mrad used for HAADF data. An energy dispersive X-ray (EDX) spectrometer in the TEM and an axis-ultra X-ray photoelectron spectrometer (Kratos-Axis Ultra System) with monochromatized Al-K $\alpha$  radiation were used to analyze the elemental composition of the samples. The Fe K-edge X-ray absorption fine structure (XAFS) spectra were recorded from beamline B18 at Diamond light source with stored electron energy of 2.2 GeV using transmission mode. The Fe K-edge spectra were processed following the conventional procedure using the IFEFFIT package. X-ray diffraction (XRD) patterns were obtained by a diffractometer (PW1830, Philips) equipped with Cu-K $\alpha$  radiation of 1.54 Å. Raman spectra were recorded with a LabRAM Aramis microscope using 532-nm excitation at room temperature. The nitrogen adsorption isotherms were recorded using an ASAP 2460 (Micromeritics) analyzer. Fourier-transform infrared spectroscopy (FTIR) measurements were performed using a VERTEX 33 spectroscopy.

#### *2.5. Electrochemical Measurements*

Electrochemical measurements were performed on an electrochemical station (CHI 660E) connected with a typical three-electrode cell. Catalyst powder was dispersed into a mixture of deionized water, isopropanol, ethylene glycol and Nafion solution (5 wt.%) with a volumetric ratio of 1000:750:150:95:5 by ultrasonication. The weight percentage of the catalyst powder in the resulting suspension was 1.6 mg mL<sup>-1</sup>. 80 uL of the

suspension was deposited onto carbon paper with a geometric area of  $10 \times 10$  mm and thoroughly dried before the electrochemical measurements. A carbon rod and Hg/HgO electrode were used as counter and reference electrodes, respectively. Linear sweeping voltammetry (LSV) measurements were performed with a scan rate of 2 mV/s. To evaluate the double-layer capacitance, cyclic voltammetry measurements were conducted with varying scan rates in the potential range of 0.15 ~ 0.25 V vs. Hg/HgO. The double-layer capacitance ( $C_{dl}$ ) was estimated by plotting  $(J_a - J_c)/2$  against scan rate, where  $J_a$  and  $J_c$  are the anodic and cathodic current densities at 0.2 V vs. Hg/HgO, respectively. Both chronoamperometry and ISTEP tests were conducted to evaluate the durability of the catalyst. Electrochemical impedance spectroscopy (EIS) tests were done from 0.1 Hz to 100 kHz with amplitude of 10 mV. The turnover frequency (TOF) was calculated by the method reported in the literature by assuming that all single Fe atoms in the electrode are active sites and accessible to the electrolyte [44]. All the polarization curves were reported with Ohmic drop correction. All the potentials reported in this work were referenced to a reversible hydrogen electrode (RHE) by following equations:  $E$  (vs. RHE) =  $E$  (vs. Hg/HgO) + 0.098 + 0.059\*pH. All the electrochemical measurements were conducted at ambient temperature.

## 2.6. Computational Methods

All DFT calculations, including structural optimizations and total energy calculations, were performed using the Vienna Ab initio Simulation Package [45] with periodic boundary conditions. We used a plane-wave basis set with a kinetic energy cutoff of 400 eV to expand the wave functions. The Perdew-Burke-Ernzerhof functional [46] in combination with Grimme's D3 van der Waals correction [47] with the Becke-Johnson damping [48], and the projector augmented wave method [49,50] were used to solve the Kohn-Sham equations. A first-order Methfessel-Paxton smearing [51] with a width of 0.2 eV was used to improve the convergence of electronic self-consistent field calculations. All DFT calculations were spin-polarized, and have been performed in the  $\Gamma$ -point approximation for sufficiently large cells; we used an  $8 \times 8$  supercell of AB-stacked bilayer graphene, with a vacuum slab of  $\sim 15$  Å thickness. An energy

convergence threshold of  $10^{-4}$  eV was used for all total energy calculations, and the structural optimizations, including cell parameters and atomic positions, were considered converged if all interatomic forces fall below 0.01 eV/Å. The Bader's charge analysis was performed using the method developed by Henkelman *et al* [52]. A range of different configurations, all featuring Fe-N<sub>x</sub> species in the top layer and an additional graphitic nitrogen in the bottom layer, with or without sulfur substitution were considered. The optimized geometries of five relevant configurations (with sulfur substitution) and the relative energies, relevant bond lengths and Bader charges on Fe atoms of these configurations were studied.

### 3. Results and Discussion

#### 3.1 Structural characterization

As schematically illustrated in **Fig. 1A**, the sample is synthesized via pyrolysis of a mixture of Hb-adsorbed BCNT in inert atmosphere. The synthesis process is simple and does not involve any sophisticated instrumentation and fabrication, which is beneficial for large-scale production. Herein, acid-treated BCNT (see **Fig. S1**) was utilized as a catalyst support because of the numerous defects and surface groups, and large surface areas, which afford prominent advantages for adsorbing Hb biomolecules and further stabilizing single metal atoms. FTIR results (**Fig. S2**) reveal the changes of the surface groups in the samples. After the pyrolysis process, most of the groups of Hb were removed except that some -OH and C=O groups are noted from the Hb-1000 and Hb/BCNT-1000 samples, indicating the transformation of Hb into carbonaceous materials. **Fig. 1B** shows the morphology of the Hb/BCNT-1000. The FESEM image shown in **Fig. 1B** presents an overview of the sample. It indicates that the sample consists of fibrous nanotubes and irregular aggregates. Such aggregates are composed of carbon nanosheets arising from the exfoliation of BCNT (see **Fig. S1d**) as confirmed by the TEM image shown in **Fig. 1C**. High-resolution TEM images (**Fig. 1D, E** and **Fig. S3b, c**) show the lattice fringes of crystallized BCNT and disorder of the amorphous carbons resulting from the pyrolysis of Hb. A HAADF scanning

transmission electron microscope (HAADF-STEM) image (**Fig. 1F**) reveals the dispersion of bright dots in the carbonaceous matrix. Aberration-corrected HAADF-STEM images (**Fig. 1G, H and Fig. S3d**) further confirm the presence of numerous bright dots which highlighted by red circles, corresponding to single Fe atoms. A few Fe nanoparticles are also observed from the sample, as shown in **Fig. S3e**. The EDX elemental maps (**Fig. S3g-j**) vividly resolve the distribution of C, N, S and Fe elements. The morphology of the Hb-1000 sample was also examined, as shown in **Fig. S4**. The sample mainly consists of carbon supported iron nanoparticles. On close inspection of aberration-corrected HAADF-STEM images (**Fig. S4**), we could not find single iron atoms. These findings suggest that the presence of BCNT is critical for the formation of single Fe atoms in the samples.

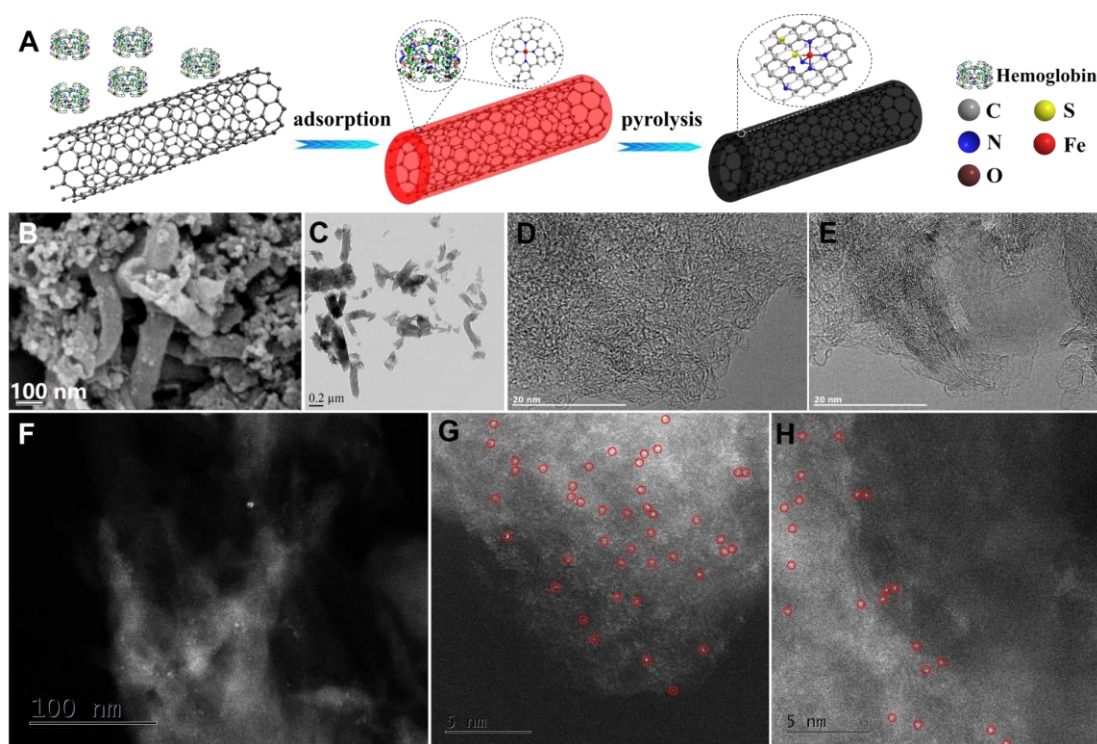


**Fig. 1.** (A) schematic illustration of the synthetic process. (B) FESEM, (C) TEM, (D, E) high-resolution TEM, (F) HAADF-STEM and (G, H) high-resolution HAADF-STEM images of Hb/BCNT-1000.

An XRD pattern of Hb/BCNT-1000 (**Fig. 2A**) shows four distinct peaks at 25.6, 43.2, 53.7 and 77.6°, corresponding to the diffraction of (200), (101), (004) and (110) planes of graphitized BCNT, respectively. Further examination of the XRD profile also

confirms a trace of metallic iron phase (PDF # 01-085-1410). Such an iron phase is also noted from the XRD profile of 80%Hb/BCNT-1100, but absent from that of 80%Hb/BCNT-900 (see **Fig. S5**), manifesting that its formation is closely related to the pyrolysis temperature. The XRD profiles of Hb-1000 show the diffractions peaks of graphitized carbon, iron and a trace of magnetite (PDF #00-011-0614).

The Brunauer-Emmett-Teller (BET) surface area and pore volume of the Hb/BCNT-1000 were determined based on the N<sub>2</sub> adsorption-desorption isotherm as shown in **Fig. 2B**. For comparison, the isotherms and corresponding analysis results of the control samples are shown in **Fig. S6-7**. The Hb/BCNT-1000 sample has a BET surface area of 261 m<sup>2</sup> g<sup>-1</sup>, which is larger than those of BCNT (52 m<sup>2</sup> g<sup>-1</sup>) and Hb-1100 (119 m<sup>2</sup> g<sup>-1</sup>). Such a large surface area is beneficial for the anchoring of Fe atoms and also the dispersion of catalytically active sites. The effect of pyrolysis temperature on the surface area was investigated. Interestingly, with increasing pyrolysis temperature, the BET value of the samples slightly increased as shown in **Fig. S7**.

The structures of the samples were studied by Raman spectra. As shown in **Fig. 2C**, all the Raman spectra display typical peaks of carbon materials, consisting of D, G, 2D and 2D' bands [53]. To quantitatively evaluate the properties of the samples, the intensity ratio of I<sub>D</sub>/I<sub>G</sub> was calculated. The BCNT exhibit an I<sub>D</sub>/I<sub>G</sub> value of 1.06, which is smaller than those of Hb/BCNT-1000 (1.64) and Hb-1000 (2.22), suggesting that the carbonaceous material resulting from the pyrolysis of Hb has more defects and a lower crystallinity [54]. The effects of pyrolysis temperature and Hb content were further investigated. The I<sub>D</sub>/I<sub>G</sub> value increases with increasing Hb content in the feedstock (see **Fig. S8**). In contrast, the effect of pyrolysis temperature is not so straightforward. The 80%Hb/BCNT-800 possesses an I<sub>D</sub>/I<sub>G</sub> value of 2.06, which is larger than those of 80%Hb/BCNT-900 (1.57), Hb/BCNT-1000 (1.64) and 80%Hb/BCNT-1100 (2.00).

The structures of the samples were also revealed by X-ray photoelectron spectroscopy (XPS). The deconvolution of high-resolution S 2p and N 1s spectra was conducted as shown in **Fig. 2D**, and **E**, respectively. It is noteworthy that five components including pyridinic N, pyrrolic N, graphitic N, oxidized N and Fe-N<sub>x</sub>

species, corresponding to binding energies of 398.5, 400.8, 401.6, 403.0 and 399.8 eV, respectively, are obtained by deconvolution of the N 1s spectrum [55]. The signal of iron is quite weak as shown in **Fig. 2F**. It is difficult to identify the electronic states of iron from the Fe 2p spectrum. **Fig. S9** shows the XPS results of Hb-1000. Notably, the N 1s spectrum of Hb-1000 does not contain the Fe-N<sub>x</sub> species, which is consistent with the absence of single iron atoms in the samples. Since the state of nitrogen plays a critical role in the catalytic performance, the N 1s spectra of the samples obtained from varying pyrolysis temperatures (**Fig. S10**) and Hb contents (**Fig. S11**) were systematically analyzed. The results are shown in **Tables S1-2**. It can be seen that the total nitrogen content, pyrrolic-N, graphitic-N and oxidized-N in the samples decrease with increasing pyrolysis temperature. On the contrary, the pyridinic-N shows an opposite trend. Note that the Hb/BCNT-1000 sample possesses a Fe-N<sub>x</sub> percentage of 15.5%, which is larger than those of 80%Hb/BCNT-900 (12.2%) and 80%Hb/BCNT-1100 (15.1%). The total nitrogen content is also affected by the Hb content in the feedstock. The Hb-1000 sample has a total nitrogen percentage of 1.06%, which is larger than those of Hb/BCNT-1000 (0.57%) and 50%Hb/BCNT-1000 (0.06%). However, it has no Fe-N<sub>x</sub> species. Though the 50%Hb/BCNT-1000 has a Fe-N<sub>x</sub> percentage of 18%, the absolute Fe-N<sub>x</sub> content is still limited owing to the negligible total nitrogen content.

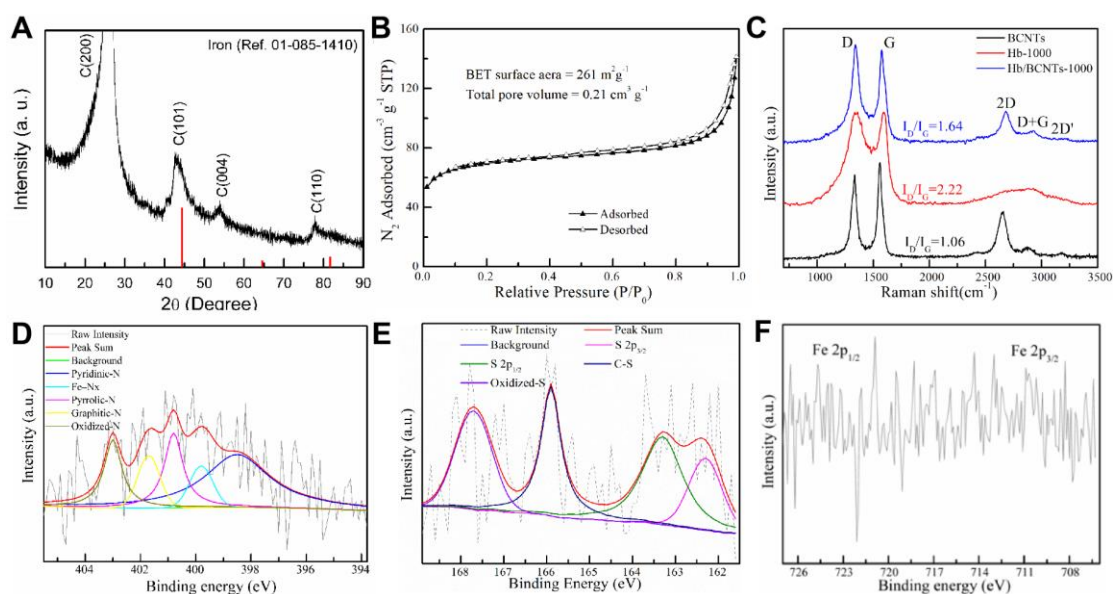


**Fig. 2.** (A) XRD pattern, (B) N<sub>2</sub> adsorption-desorption isotherm, (C) Raman spectra,

and (D-H) XPS spectra of N 1s, S 2p and Fe 2p of the samples.

To further confirm the Fe-N<sub>x</sub> active sites and investigate their chemical states and coordination environment in Hb/BCNT-1000 at the atomic level, XAFS measurements were performed. The normalized Fe K-edge X-ray absorption near edge structure (XANES) spectra of Fe foil, Fe<sub>2</sub>O<sub>3</sub> and Hb/BCNT-1000 are shown in **Fig. 3A**. It can be seen that the position of the absorption edge for Hb/BCNT-1000 is located between Fe foil and Fe<sub>2</sub>O<sub>3</sub>, indicating that the oxidation state of iron in Hb/BCNT-1000 is between Fe<sup>0</sup> and Fe<sup>3+</sup> [56,57]. The unique electronic structure of Fe species with positive charges is mainly due to the coordination of Fe and N in the sample [57]. **Fig. 3B** shows the k<sup>3</sup>-weighted Fourier transform spectra in R space of the Fe K-edge extended X-ray absorption fine structure (EXAFS) for the samples. The EXAFS curve of Hb/BCNT-1000 is clearly different from those of the references. Two distinct peaks were observed at 1.51 and 2.21 Å. The peak located at 1.51 Å is ascribed to the Fe-N first coordination shell, indicating that the iron atoms in Hb/BCNT-1000 are isolated by nitrogen [31,58]. The peak located at 2.21 Å is similar to the Fe-Fe first coordination shell of Fe foil reference, suggesting the existence of iron nanoparticles, which is consistent with the results of the aberration-corrected HAADF-STEM. Wavelet transform (WT) analysis was performed to gain a radial distance resolution and resolution in k space of Fe species. The WT contour plots of Fe K-edge EXAFS for Hb/BCNT-1000 are significantly different from those of references as shown in **Fig. 3C**. The WT contour plots of Hb/BCNT-1000 could be divided into two intensity maxima at 8.0 and 4.8 Å<sup>-1</sup>, corresponding to Fe nanoparticles and Fe-N<sub>x</sub> species, respectively [58,59]. This is consistent with the results of k<sup>3</sup>-weighted Fourier transform spectra in R space. EXAFS fitting (**Fig. 3C and D**) was performed to reveal the coordination structure of Fe-N<sub>x</sub> species. The best fitting results show that the average coordination number was estimated to be 3.2 for Fe-Fe and 5.1 for Fe-N<sub>x</sub> species, and that the average bond distances of Fe-Fe and Fe-N are 2.57 and 2.07 Å (**Table S3**), respectively. Based on the spectral results and EXAFS fitting, it can be concluded that each single iron atom in Hb/BCNT-1000 is coordinated by five atoms and that the resulting Fe-N<sub>x</sub> species is

stabilized by the nitrogen and sulfur co-doped carbon matrix, affording the active sites for the OER.

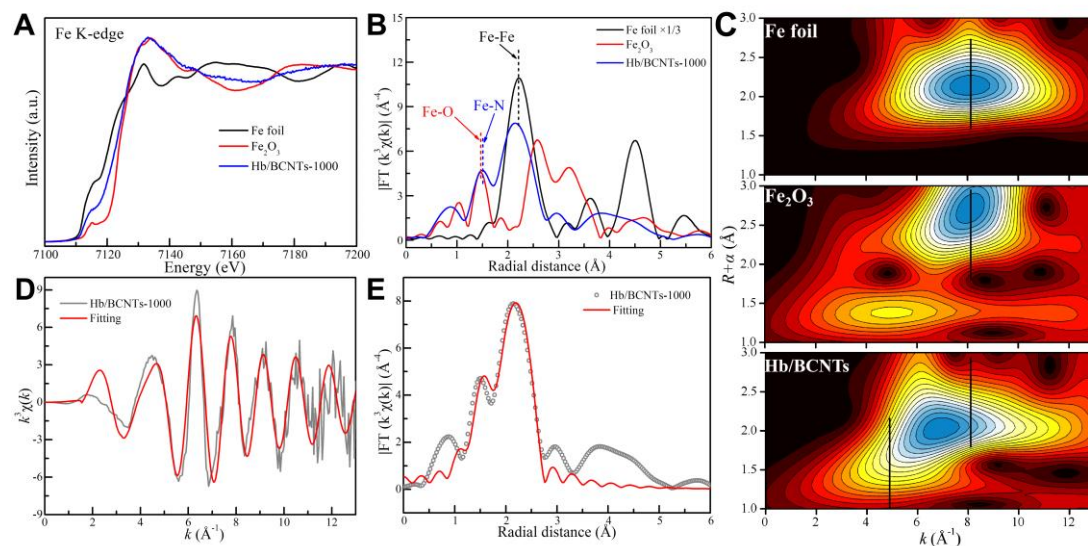


**Fig. 3.** Synchrotron XAFS measurement of Hb/BCNT-1000 catalyst. (A) Fe K-edge XANES spectra of Hb/BCNT-1000 catalyst and reference samples, (B)  $k^3$ -weighted Fourier transform spectra from Fe K edge EXAFS, (C) WT for the  $k^3$ -weighted EXAFS signal, and (D, E) Corresponding EXAFS fitting curves in  $k$  and  $R$  space, respectively.

### 3.2 Electrochemical activity

The electrochemical activity of the samples was first evaluated by LSV. **Fig. 4A** shows the LSV curves recorded in 1 M KOH with a scan rate of  $2 \text{ mV s}^{-1}$ . For comparison, the activity of the samples was benchmarked against a commercial  $\text{IrO}_2$  electrocatalyst. The BCNT and Hb-1000 samples show limited current densities throughout the tested potential range. At potentials less than 1.56 V,  $\text{IrO}_2$  possesses higher current densities relative to the Hb/BCNT-1000 sample. At higher potentials, the Hb/BCNT-1000 outperforms  $\text{IrO}_2$  and the discrepancies of current density increase with increasing potential. Specifically, to yield a current density of  $10 \text{ mA cm}^{-2}$ , the Hb/BCNT-1000 requires an overpotential of 326 mV, which is slightly higher than that of  $\text{IrO}_2$  (322 mV), but significantly lower than those of BCNT (526 mV) and Hb-1000 (551 mV). At an applied overpotential of 380 mV, the Hb/BCNT-1000 possesses a current density of  $83.6 \text{ mA cm}^{-2}$ , which is much larger than those of the BCNT ( $1.98$

$\text{mA cm}^{-2}$ ), Hb-1000 ( $1.47 \text{ mA cm}^{-2}$ ) and  $\text{IrO}_2$  ( $32.8 \text{ mA cm}^{-2}$ ) as shown in **Fig. 4B**. It is worth noting that such performance of Hb/BCNT-1000 is better than most non-precious OER electrocatalysts reported in the literature as shown in **Table S4**. The Tafel slopes of the samples were determined based on the LSV curves as shown in **Fig. 4C**. The Hb/BCNT-1000 exhibits a Tafel slope of  $40.2 \text{ mV dec}^{-1}$ , which is smaller than those of  $\text{IrO}_2$  ( $45.6 \text{ mV dec}^{-1}$ ), BCNT ( $169 \text{ mV dec}^{-1}$ ) and Hb-1000 ( $173 \text{ mV dec}^{-1}$ ), indicative of its promising prospect for practical applications. For better comparison, TOF values of the samples were also calculated as shown in **Fig. S12**. They reveal that the Hb/BCNT-1000 has much larger TOF values than  $\text{IrO}_2$  and Hb-1000. To explore the origin of the superior activity of the Hb/BCNT-1000, the  $C_{dl}$  of the sample, which is well correlated with the electrochemical active surface area, was determined by cyclic voltammetry curves recorded in a potential range of  $0.15\sim 0.25 \text{ V}$  with varying scan rates, as shown in **Fig. S13**. There is a good linear relationship between the scan rate and  $(j_a - j_c)/2$ , as shown in **Fig. 4D**. The  $C_{dl}$  values of Hb/BCNT-1000 was determined to be  $5.33 \text{ mF cm}^{-2}$ , which is slightly larger than those of BCNT ( $4.28 \text{ mF cm}^{-2}$ ) and Hb-1000 ( $3.35 \text{ mF cm}^{-2}$ ). Given the remarkable differences in current densities of the three samples (see **Fig. 4A**), it can be concluded that the electrochemical active area of the sample is not the major reason for the superior activity of Hb/BCNT-1000. The activity of the sample was further evaluated by EIS as shown in **Fig. 4E** and the series resistance ( $R_s$ ) and charge transfer resistance of the catalyst-electrolyte interface ( $R_{ct}$ ) were determined accordingly. The  $R_s$  value of the BCNT was determined to be  $1.61 \Omega$ , which is smaller than those of Hb-1000 ( $1.83 \Omega$ ), Hb/BCNT-1000 ( $1.91 \Omega$ ) and  $\text{IrO}_2$  ( $2.45 \Omega$ ), owing to its outstanding electron conductivity. The  $R_{ct}$  value of Hb/BCNT-1000 was only  $0.66 \Omega$ , which is smaller than those of  $\text{IrO}_2$  ( $0.75 \Omega$ ), BCNT ( $8.76 \Omega$ ) and Hb-1000 ( $11.34 \Omega$ ), indicating the fast kinetics of OER over the sample. The stability of the Hb/BCNT-1000 sample was evaluated by ISTEP measurement, as shown in **Fig. 4F**. With increasing current densities from  $20$  to  $50 \text{ mA cm}^{-2}$ , the potential at each current step is quite stable, manifesting the excellent stability of the sample. The durability of Hb/BCNT-1000 was further studied by chronoamperometric measurements as shown in **Fig. S14**. At overpotentials of  $350$  and  $380 \text{ mV}$ , the corresponding current densities

are stable, which is consistent with the ISTEP results. The morphology of the spent Hb/BCNT-1000 was examined, as shown in **Fig. S15**. It reveals that the spent samples well preserve the structures. Further inspection of high-resolution HAADF-STEM images (see **Fig. S15c**) confirms the presence of many single iron atoms, as marked by red circles. This finding suggests that nitrogen-stabilized single iron atoms in the samples are sufficiently stable to survive through the long-term electrochemical measurements. The structure of the spent Hb/BCNT-1000 was also investigated by XPS, as shown in **Fig. S16**. Compared with XPS spectra of the fresh Hb/BCNT-1000 (see **Fig. 2**), C 1s, O1s, N 1s and Fe 2p of the spent sample show limited variations. Only the S 2p spectrum varied significantly. The relative content of the oxidized-S component in the spent sample increases. This could be attributed to the possible role of sulfur on stabilizing single iron atoms.

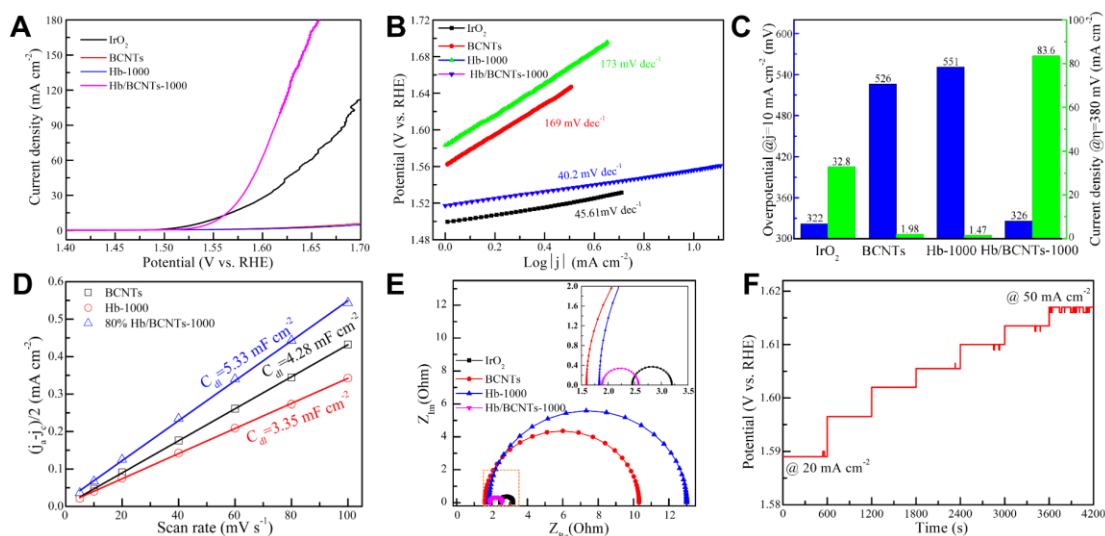


**Fig. 4.** (A) LSV curves recording in 1 M KOH with a scan rate of  $2 \text{ mV s}^{-1}$ , (B) corresponding Tafel slopes, (C) comparison on the catalytic activity, (D) plots of  $(j_a - j_c)/2$  vs. scan rate, (E) electrochemical impedance spectra, and (F) ISTEP result of the samples.

### 3.3 Theoretical calculation

The superior catalytic activity of Hb/BCNT-1000 can be explained from three aspects. First, abundant active Fe-N<sub>x</sub> sites available in the sample play a crucial role in

the superior activity. Secondly, the presence of sulfur could further enhance the activity of Fe-N<sub>x</sub> species. Previous studies suggested that the metal atoms in the Fe-N<sub>x</sub> species possess high adsorption free energies of H<sub>2</sub>O and oxygen-containing intermediates due to higher positive charge on Fe as a result of the strong electron-negativity of neighboring nitrogen atoms, thus compromising their OER activity [14]. Since the electronegativity of sulfur (2.58 on Pauling scale) is weaker than that of nitrogen (3.04 on Pauling scale), the introduction of foreign sulfur atoms in the carbon matrix could modify the electronic structure of Fe-N<sub>x</sub> species, enriching the electron density of the iron atoms, which would reduce the potential barriers and improve the OER kinetics [60,61]. Using AB-stacked bilayer graphene (BLG) as a model system, we performed DFT calculations with periodic boundary conditions (see the details in the computational method) to understand the role of sulfur as a co-dopant. The first question that needs to be addressed is the location of sulfur atoms within BLG. We considered several configurations with sulfur atoms located at different sites. The optimized geometries of five relevant configurations are shown in **Fig. 5**. The relative energies, relevant bond lengths and Bader charges on Fe atoms of these configurations were summarized in **Table S5**. The values of a configuration without sulfur substitution (config-0, Fe-N<sub>4</sub> species) are also listed for comparison. It turns out that the Fe-N<sub>3</sub>S-N structural motif (See config-1 in **Fig. 5**) represents the most energetically favorable configuration. Comparing with the Fe-N<sub>4</sub>-S (see config-1 in **Fig. 5**), the Fe-N<sub>3</sub>S-N configuration lowers the overall energy of the system by 46 kJ mol<sup>-1</sup>, indicating that sulfur tends to form direct chemical bond with iron within the porphyrin-like Fe-N<sub>3</sub>S species. Our calculation results confirm the formation of a chemical bond between sulfur and iron atoms, which is consistent with the results reported by Zhang *et al* [62]. The Fe-S bond length in our optimized Fe-N<sub>3</sub>S-N configuration is 2.0 Å, which is close to that of Fe-N (~1.9 Å). Considering that the sulfur content (0.09 wt.%) is significantly lower than that of nitrogen (0.57 wt.%) in our sample, the presence of Fe-S bonding in our sample cannot be excluded based on the EXAFS data alone (see **Fig. 3B**). Having determined the preferential location of sulfur, the next question is how sulfur affects the electronic properties of the center iron atoms which serve as the active site for the OER.

To this end, we performed Bader charge analysis on both Fe-N<sub>4</sub>-N and Fe-N<sub>3</sub>S-N moieties. The results suggest that the partial atomic charge of iron decreases from +1.08 (in Fe-N<sub>4</sub>) to +0.82 (in Fe-N<sub>3</sub>S-N) by replacing nitrogen with less electronegative sulfur. In other words, the electron-donating iron atoms become less positive by the sulfur substitution, which may improve the OER activity of the sample [36]. Overall, our calculations indicate the activity of SACs can be tailored through nitrogen and sulfur co-doping of carbon matrix due to formation of metal-sulfur bonds which modifies the electronic properties of SACs, leading to enhanced OER activity. Lastly, the excellent conductivity and large surface area of the BCNT support are also favorable for the superior OER activity of Hb/BCNT-1000. The abundant defects in the BCNT played a decisive role in stabilizing the single iron atoms as shown in the aforementioned discussion.

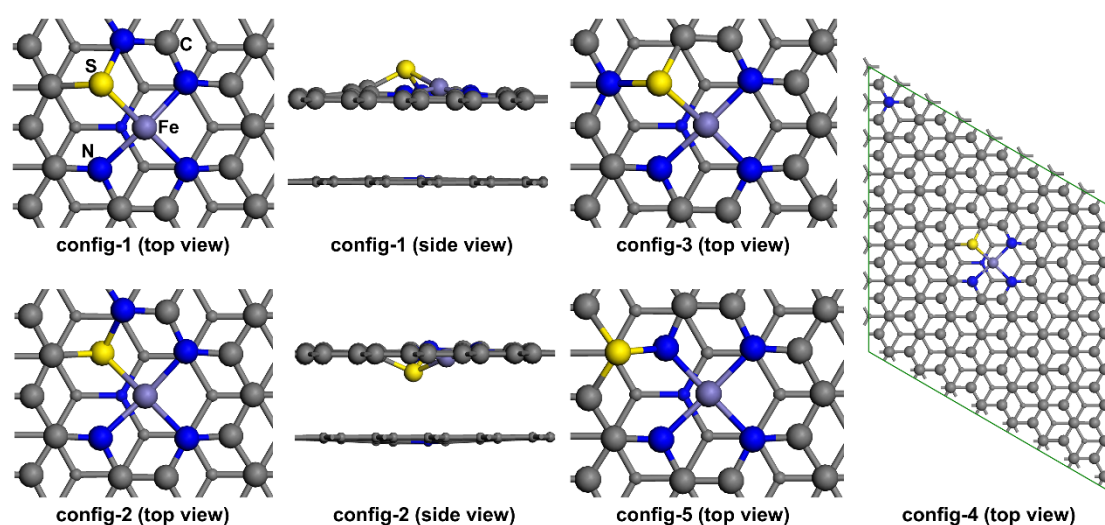


**Fig. 5.** DFT optimized geometries of selected configurations. The atoms in the top and bottom layers are represented by large and small balls, respectively. Only part of the structural model is shown for clarity (except config-4 of which the full structural model is shown). Color code of different atoms is indicated in the figure.

### 3.4 Effects of feedstock and pyrolysis temperature

The effects of pyrolysis temperature and Hb content on the catalytic activity were also explored. **Fig. S17a** shows the LSV curves of the samples prepared with varying

Hb content in the feedstock. Among the samples, the Hb/BCNT-1000 exhibits the highest current densities. TOF values of the samples show a similar trend (see **Fig. S17b**). The EIS results reveal that the  $R_{ct}$  values of the samples follow the sequence of Hb/BCNT-1000 < 90%Hb/BCNT-1000 < 70%Hb/BCNT-1000 < 50%Hb/BCNT-1000 < 95%Hb/BCNT-1000 < Hb-1000, which is consistent with the LSV results. **Fig. S18** shows the effects of pyrolysis temperature on the electrochemical activity. It reveals that the Hb/BCNT-1000 has the largest current densities and TOF values, and smallest  $R_{ct}$  values. The activity of the samples is well correlated with the content of Fe-N<sub>x</sub> species as shown in **Table S2**, which unambiguously suggests that the Fe-N<sub>x</sub> is the active site for OER reaction.

#### **4. Conclusion**

In summary, we reported a facile synthetic protocol to prepare single isolated iron atoms anchored to nitrogen-sulfur-codoped carbon matrix via pyrolyzing the mixture of Hb and BCNT. The composition of iron and nitrogen can be readily tuned by varying the Hb content in the feedstock and pyrolysis temperature. Among the samples, the Hb/BCNT-1000 sample possessed the best catalytic performance, which outperformed the benchmark of IrO<sub>2</sub> at an overpotential of 380 mV. The X-ray absorption fine structure analyses indicated that the Fe-N<sub>x</sub> species in the sulfur doped carbon matrix are the active sites. DFT calculations suggested pronounced electronic modification of iron arisen from the presence of sulfur. The superior catalytic performance of Hb/BCNT-1000 could be related to the abundant Fe-N<sub>x</sub> species and the presence of sulfur dopants which further modified the electronic structure of the single Fe atoms. This work exemplifies a value-added utilization of Hb. It possibly affords a new route to convert animal blood waste from slaughterhouses into valuable products. Owing to the simplicity, the synthetic strategy reported in this work could be extended to prepare other MNCs by varying biomolecule precursors and supports.

#### **Declaration of competing interest**

The authors declare no conflict of interest.

## **Acknowledgement**

The project was financially supported by the National Natural Science Foundation of China (Grant No. 21706081) and 111 Project (B17018). The authors thank Diamond Light Source for the support from the electron Physical Science Imaging Centre for the use of Instrument E01 under proposal number MG23723. The authors thanks to Professors Alan Chadwick and Giannantonio Cibin for the XAS measurements, and the Diamond Light Source for provision of beam time through the Block Allocation Group (BAG) for Energy Materials under proposal sp17198. Dr Luo acknowledges the support of a Daphne Jackson Trust fellowship and its sponsors are Royal Academy of Engineering and the University of Nottingham. Dr Ling acknowledges the use of the Athena supercomputer through the HPC Midlands+ Consortium, and the ARCHER supercomputer through membership of the UK's HPC Materials Chemistry Consortium, which are funded by EPSRC Grants No. EP/P020232/1 and No. EP/R029431/1, respectively. Dr Fernandes thanks Beacons of Excellence: Propulsion Futures for the financial support.

## **Appendix A. Supplementary data**

Further Structural characterizations and calculation results were included in the Supporting Information.

## **References**

- [1] Z.W. Seh, J. Kibsgaard, C.F. Dickens, I. Chorkendorff, J.K. Nørskov, T.F. Jaramillo, Combining theory and experiment in electrocatalysis: Insights into materials design, *Science* 355 (2017) 4998.
- [2] Y.J. Chen, S.F. Ji, C. Chen, Q. Peng, D.S. Wang, Y.D. Li, Single-Atom Catalysts: Synthetic Strategies and Electrochemical Applications, *Joule* 2 (2018) 1242-1264.
- [3] L. Liang, H. Cheng, F.C. Lei, J. Han, S. Gao, C.M. Wang, *et al.*, Metallic Single-Unit-Cell Orthorhombic Cobalt Diselenide Atomic Layers: Robust Water-Electrolysis Catalysts, *Angew. Chem. Int. Ed.* 54 (2015) 12004-12008.
- [4] S. Sultan, J.N. Tiwari, A.N. Singh, S. Zhumagali, M. Ha, C.W. Myung, *et al.*, Single Atoms and Clusters Based Nanomaterials for Hydrogen Evolution, Oxygen Evolution Reactions, and Full

Water Splitting, *Adv. Energy Mater.* 9 (2019) 1900624.

[5] F. Song, L.C. Bai, A. Moysiadou, S. Lee, C. Hu, L. Liardet, X.L. Hu, Transition Metal Oxides as Electrocatalysts for the Oxygen Evolution Reaction in Alkaline Solutions: An Application-Inspired Renaissance, *J. Am. Chem. Soc.* 140 (2018) 7748-7759.

[6] J.F. Zhang, J.Y. Liu, L.F. Xi, Y.F. Yu, N. Chen, S.H. Sun, *et al.*, Single-Atom Au/NiFe Layered Double Hydroxide Electrocatalyst: Probing the Origin of Activity for Oxygen Evolution Reaction, *J. Am. Chem. Soc.* 140 (2018) 3876-3879.

[7] H.L. Fei, J.C. Dong, Y.X. Feng, C.S. Allen, C.Z. Wan, B. Voloskiy, *et al.*, General synthesis and definitive structural identification of MN<sub>4</sub>C<sub>4</sub> single-atom catalysts with tunable electrocatalytic activities, *Nat. Catal.* 1 (2018) 63-72.

[8] J.Y. Liu, Catalysis by Supported Single Metal Atoms, *ACS Catal.* 7 (2017) 34-59.

[9] G. Vilé, D. Albani, M. Nachtegaal, Z.P. Chen, D. Dontsova, M. Antonietti, *et al.*, A Stable Single-Site Palladium Catalyst for Hydrogenations, *Angew. Chem. Int. Ed.* 54 (2015) 11265-11269.

[10] E.C. Tyo, S. Vajda, Catalysis by clusters with precise numbers of atoms, *Nat. Nanotechnol.* 10 (2015) 577-588.

[11] X.J. Cui, W. Li, P. Ryabchuk, K. Junge, M. Belle, Bridging homogeneous and heterogeneous catalysis by heterogeneous single-metal-site catalysts, *Nat. Catal.* 1 (2018) 385-397.

[12] H.X. Xu, D.J. Cheng, D.P. Cao, X.C. Zeng, A universal principle for a rational design of single-atom electrocatalysts, *Nat. Catal.* 1 (2018) 339-348.

[13] X.Y. Li, H.P. Rong, J.T. Zhang, D.S. Wang, Y.D. Li, Modulating the local coordination environment of single-atom catalysts for enhanced catalytic performance, *Nano Res.* (2020)

[14] Q. Xu, C.X. Guo, S.B. Tian, J. Zhang, W.X. Chen, W.-C. Cheong, *et al.*, Coordination structure dominated performance of single-atomic Pt catalyst for anti-Markovnikov hydroboration of alkenes, *Science China Mater.* (2020)

[15] Y. Li, H.J. Wen, J. Yang, Y.Z. Zhou, X.N. Cheng, Boosting oxygen reduction catalysis with N, F, and S tri-doped porous graphene: Tertiary N-precursors regulates the constitution of catalytic active sites, *Carbon* 142 (2019) 1-12.

[16] Y.F. Chen, Z.J. Li, Y.B. Zhu, D.M. Sun, X.E. Liu, L. Xu, *et al.*, Atomic Fe Dispersed on N-Doped Carbon Hollow Nanospheres for High-Efficiency Electrocatalytic Oxygen Reduction, *Adv. Mater.* 31 (2019) 1806312.

- [17] C.Z. Zhu, S.F. Fu, Q.R. Shi, D. Du, Y.H. Lin, Single-Atom Electrocatalysts, *Angew. Chem. Int. Ed.* 56 (2017) 13944-13960.
- [18] I. Roger, M.A. Shipman, M.D. Symes, Earth-abundant catalysts for electrochemical and photoelectrochemical water splitting, *Nat. Rev. Chem.* 1 (2017) 0003.
- [19] M. Dhiman, V. Polshettiwar, Supported Single Atom and Pseudo-Single Atom of Metals as Sustainable Heterogeneous Nanocatalysts, *ChemCatChem* 10 (2018) 881-906.
- [20] Z.P. Zhang, J.T. Sun, F. Wang, L.M. Dai, Efficient Oxygen Reduction Reaction (ORR) Catalysts Based on Single Iron Atoms Dispersed on a Hierarchically Structured Porous Carbon Framework, *Angew. Chem. Int. Ed.* 57 (2018) 9038-9043.
- [21] S.Q. Hu, W.P. Ni, D.H. Yang, C. Ma, J.H. Zhang, J.F. Duan, *et al.*, Fe<sub>3</sub>O<sub>4</sub> nanoparticles encapsulated in single-atom Fe-N-C towards efficient oxygen reduction reaction: Effect of the micro and macro pores, *Carbon* 162 (2020) 245-255.
- [22] H.B. Zhang, P.F. An, W. Zhou, B.Y. Guan, P. Zhang, J.C. Dong, *et al.*, Dynamic traction of lattice-confined platinum atoms into mesoporous carbon matrix for hydrogen evolution reaction, *Sci. Adv.* 4 (2018) 6657.
- [23] B.Z. Lu, L. Guo, F. Wu, Y. Peng, J.E. Lu, T.J. Smart, *et al.*, Ruthenium atomically dispersed in carbon outperforms platinum toward hydrogen evolution in alkaline media, *Nat. Commun.* 10 (2019) 631.
- [24] X.L. Xu, R. Si, A.I. Rykov, J.H. Wang, S.S. Yu, S.L. Wang, *et al.*, Insight into the role of Ni-Fe dual sites in the oxygen evolution reaction based on atomically metal-doped polymeric carbon nitride, *J. Mater. Chem. A* 7 (2019) 14001-14010.
- [25] Y.X. Ding, A. Klyushin, X. Huang, T. Jones, D. Teschner, F. Girgsdies, T. Rodenas, R. Schlogl, S. Heumann, Cobalt-Bridged Ionic Liquid Polymer on a Carbon Nanotube for Enhanced Oxygen Evolution Reaction Activity, *Angew. Chem. Int. Ed.* 57 (2018) 3514-3518.
- [26] Y. Zheng, Y. Jiao, Y.H. Zhu, Q.R. Cai, A. Vasileff, L.H. Li, *et al.* Molecule-Level g-C<sub>3</sub>N<sub>4</sub> Coordinated Transition Metals as a New Class of Electrocatalysts for Oxygen Electrode Reactions, *J. Am. Chem. Soc.* 139 (2017) 3336-3339.
- [27] P.-L. Lu, Y.J. Yang, J.N. Yao, M. Wang, S. Dipazir, M.L. Yuan, *et al.*, Facile synthesis of single-nickel-atomic dispersed N-doped carbon framework for efficient electrochemical CO<sub>2</sub> reduction, *Applied Catal. B: Environ.* 241 (2019) 113-119.

- [28] Z.K. Yang, C.Z. Yuan, A.W. Xu, Confined Pyrolysis within a Nanochannel to Form a Highly Efficient Single Iron Site Catalyst for Zn–Air Batteries, *ACS Energy Lett.* 3 (2018) 2383-2389.
- [29] J. Zhao, Q.M. Deng, S.M. Avdoshenko, L. Fu, J. Eckert, M.H. Rummeli, Direct in situ observations of single Fe atom catalytic processes and anomalous diffusion at graphene edges, *Proc. Natl. Acad. Sci. U.S.A.* 111 (2014) 15641-15646.
- [30] X.L. Wang, J. Du, Q.H. Zhang, L. Gu, L.J. Cao, H.-P. Liang, In situ synthesis of sustainable highly efficient single iron atoms anchored on nitrogen doped carbon derived from renewable biomass, *Carbon* 157 (2020) 614-621.
- [31] L. Jiao, H.L. Jiang, Metal-Organic-Framework-Based Single-Atom Catalysts for Energy Applications, *Chem* 5 (2019) 786-804.
- [32] T. He, S.M. Chen, B. Ni, Y. Gong, Z. Wu, L. Song, *et al.*, Zirconium-Porphyrin-Based Metal-Organic Framework Hollow Nanotubes for Immobilization of Noble-Metal Single Atoms, *Angew. Chem. Int. Ed.* 57 (2018) 3493-3498.
- [33] S. Gadipelli, T.T. Zhao, S.A. Shevlin, Z.X. Guo, Switching effective oxygen reduction and evolution performance by controlled graphitization of a cobalt-nitrogen-carbon framework system, *Energy Environ. Sci.* 9 (2016) 1661-1667.
- [34] X.Z. Fang, Q.C. Shang, Y. Wang, L. Jiao, T. Yao, Y.F. Li, *et al.*, Single Pt Atoms Confined into a Metal-Organic Framework for Efficient Photocatalysis, *Adv. Mater.* 30 (2018) 1705112.
- [35] Z.B. Liang, C. Qu, D.G. Xia, R.Q. Zou, Q. Xu, Atomically Dispersed Metal Sites in MOF-Based Materials for Electrocatalytic and Photocatalytic Energy Conversion, *Angew. Chem. Int. Ed.* 57 (2018) 9604-9633.
- [36] Z.G. Geng, Y.J. Cao, W.X. Chen, X.D. Kong, Y. Liu, T. Yao, *et al.*, Regulating the coordination environment of Co single atoms for achieving efficient electrocatalytic activity in CO<sub>2</sub> reduction, *Applied Catal. B: Environ.* 240 (2019) 234-240.
- [37] X.F. Yang, A.Q. Wang, B.T. Qiao, J. Li, J.Y. Liu, T. Zhang, Single-Atom Catalysts: A New Frontier in Heterogeneous Catalysis, *Acc. Chem. Res.* 46 (2013) 1740-1748.
- [38] A. Kulkarni, S. Siahrostami, A. Patel, J.K. Nørskov, Understanding Catalytic Activity Trends in the Oxygen Reduction Reaction, *Chem. Rev.* 118 (2018) 2302-2312.
- [39] W. Zhang, W.T. Zheng, Single Atom Excels as the Smallest Functional Material, *Adv. Funct. Mater.* 26 (2016) 2988-2993.

- [40] C.S.F. Bah, A.A. Bekhit, A. Carne, M.A. McConnell, Slaughterhouse Blood: An Emerging Source of Bioactive Compounds, *Compr. Rev. Food. Sci.* 12 (2013) 314-331.
- [41] Y. Shen, A.C. Lua, Synthesis of Ni and Ni-Cu supported on carbon nanotubes for hydrogen and carbon production by catalytic decomposition of methane, *Applied Catal. B: Environ.* 164 (2015) 61-69.
- [42] Y. Shen, A.C. Lua, A facile method for the large-scale continuous synthesis of graphene sheets using a novel catalyst, *Sci. Rep.* 3 (2013) 3037.
- [43] J.S. Wang, J.Y. Xi, Y.X. Bai, Y. Shen, J. Sun, L.Q. Chen, *et al.*, Structural designing of Pt-CeO<sub>2</sub>/CNTs for methanol electro-oxidation, *J. Power Sources* 164 (2007) 555-560.
- [44] Y.R. Xue, B.L. Huang, Y.P. Yi, Y. Guo, Z.C. Zuo, Y.J. Li, *et al.*, Anchoring zero valence single atoms of nickel and iron on graphdiyne for hydrogen evolution, *Nat. Commun.* 9 (2018) 1460.
- [45] G. Kresse, J. Furthmuller, Efficient iterative schemes for ab initio total-energy calculations using a plane-wave basis set, *Phys. Rev. B* 54 (1996) 11169-11186.
- [46] J.P. Perdew, K. Burke, M. Ernzerhof, Generalized gradient approximation made simple, *Phys. Rev. Lett.* 77 (1996) 3865-3868.
- [47] S. Grimme, J. Antony, S. Ehrlich, H. Krieg, A consistent and accurate ab initio parametrization of density functional dispersion correction (DFT-D) for the 94 elements H-Pu, *J. Chem. Phys.* 132 (2010) 154104.
- [48] S. Grimme, S. Ehrlich, L.J. Goerigk, Effect of the Damping Function in Dispersion Corrected Density Functional Theory, *Computat. Chem.* 32 (2011) 1456-1465.
- [49] P.E. Blochl, Projector augmented-wave method, *Phys. Rev. B* 50 (1994) 17953-17979.
- [50] D. Hobbs, G. Kresse, Hafner, Fully unconstrained noncollinear magnetism within the projector augmented-wave method, *J. Phys. Rev. B* 62 (2000) 11556-11570.
- [51] M. Methfessel, A.T. Paxton, High-precision sampling for Brillouin-zone integration in metals, *Phys. Rev. B* 40 (1989) 3616-3621.
- [52] G. Henkelman, A. Arnaldsson, H. Jonsson, A fast and robust algorithm for Bader decomposition of charge density, *Computat. Mater. Sci.* 36 (2006) 354-360.
- [53] A. Dimiev, D.V. Kosynkin, Al. Sinitskii, A. Slesarev, Z.Z. Sun, J.M. Tour, Layer-by-Layer Removal of Graphene for Device Patterning, *Science* 331 (2011) 1168-1172.
- [54] L.Y. Jiao, L. Zhang, X.R. Wang, G. Diankov, H.J. Dai, Narrow graphene nanoribbons from

carbon nanotubes, *Nature* 458 (2009) 877-880.

[55] J. Li, S.G. Chen, N. Yang, M.M. Deng, S. Ibraheem, J.H. Deng, *et al.*, Ultrahigh-Loading Zinc Single-Atom Catalyst for Highly Efficient Oxygen Reduction in Both Acidic and Alkaline Media, *Angew. Chem. Int. Ed.* 58 (2019) 7035-7039.

[56] X.N. Li, X. Huang, S.B. Xi, S. Miao, J. Ding, W.Z. Cai, *et al.*, Single Cobalt Atoms Anchored on Porous N-Doped Graphene with Dual Reaction Sites for Efficient Fenton-like Catalysis, *J. Am. Chem. Soc.* 140 (2018) 12469-12475.

[57] Y.Q. Zhu, W.M. Sun, J. Luo, W.X. Chen, T. Cao, L.R. Zheng, *et al.*, A cocoon silk chemistry strategy to ultrathin N-doped carbon nanosheet with metal single-site catalysts, *Nat. Commun.* 9 (2018) 3861.

[58] L. Zhao, Y. Zhang, L.B. Huang, X.Z. Liu, Q.H. Zhang, C. He, *et al.*, Cascade anchoring strategy for general mass production of high-loading single-atomic metal-nitrogen catalysts, *Nat. Commun.* 10 (2019) 1278.

[59] Y.J. Chen, S.F. Ji, Y.G. Wang, J.C. Dong, W.X. Chen, Z. Li, *et al.*, Isolated Single Iron Atoms Anchored on N-Doped Porous Carbon as an Efficient Electrocatalyst for the Oxygen Reduction Reaction, *Angew. Chem. Int. Ed.* 56 (2017) 6937-6941.

[60] H.J. Shen, E. Gracia-Espino, J.Y. Ma, K.T. Zang, J. Luo, L. Wang, *et al.*, Synergistic Effects between Atomically Dispersed Fe–N–C and C–S–C for the Oxygen Reduction Reaction in Acidic Media, *Angew. Chem. Int. Ed.* 56 (2017) 13800-13804.

[61] Y. Hou, M. Qiu, M.G. Kim, P. Liu, G. Nam, T. Zhang, *et al.*, Atomically dispersed nickel-nitrogen-sulfur species anchored on porous carbon nanosheets for efficient water oxidation, *Nat. Commun.* 10 (2019) 1392.

[62] J.T. Zhang, M. Zhang, Y. Zeng, J.S. Chen, L.X. Qiu, H. Zhou, *et al.*, Fe<sub>2</sub>N/S/N codecorated hierarchical porous carbon nanosheets for trifunctional electrocatalysis, *Small* 15 (2019) 1900307.